International Journal of Rail Transportation

ISSN: (Print) (Online) Journal homepage: www.tandfonline.com/journals/tjrt20

Suspension parameter optimization for high-speed train with severe tread wear

Hu Li, Yuan Yao & Xiangwang Chen

To cite this article: Hu Li, Yuan Yao & Xiangwang Chen (23 Apr 2024): Suspension parameter optimization for high-speed train with severe tread wear, International Journal of Rail Transportation, DOI: 10.1080/23248378.2024.2345683

To link to this article: https://doi.org/10.1080/23248378.2024.2345683

Published online: 23 Apr 2024.

INTERNATIONAL JOURNAL OF RAIL TRANSPORTATION
https://doi.org/10.1080/23248378.2024.2345683

Suspension parameter optimization for high-speed train with severe tread wear

Hu Li, Yuan Yao and Xiangwang Chen

State Key Laboratory of Rail Transit Vehicle System, Southwest Jiaotong University, Chengdu, China

ABSTRACT

The suspension parameters are optimized to improve the dynamic performance of high-speed train with severe tread wear and suppress the formation of severe tread wear. Except for the common indicator of high-conicity stability (A_{high}) for the vehicle dynamic performance with severe tread wear, a hollow wear index (HWI) is proposed to reduce the development rate of wheel hollow wear. Moreover, the low-conicity ride comfort (W_{low}) is considered for the dynamics performance with new tread. Yaw stiffness (*YS*) and the ratio of yaw damping to lateral damping (*RYL*) are proposed to characterize the suspension parameters matching. Results show that HWI is strongly positively correlated with W_{low}, and is negatively correlated with A_{high}. Increasing the *RYL* can enhance W_{low}, and the *YS* should be reduced to improve HWI under the condition of sufficient hunting stability margin. Hunting bifurcation analysis elucidates that the model with better HWI is easy to form supercritical bifurcation.

ARTICLE HISTORY
Received 3 February 2024
Revised 12 April 2024
Accepted 16 April 2024

KEYWORDS
High-speed train; tread wear; suspension parameter optimization; wheel hollow wear; hunting bifurcation

1. Introduction

The stability of high-speed trains is generally reliable under normal scenarios, but severe tread wear can occur over the course of prolonged operation [1], which leads to frame vibration acceleration alarms and other issues, seriously affecting operational safety. The severe tread wear observed in the turning repair cycle of wheel is primarily wheel hollow wear, which is mainly due to the excellent stability of high-speed trains, causing a narrow contact bandwidth. The narrow contact bandwidth can be considered as a side effect of the high stability [2]. To ensure the dynamic performance of high-speed trains, suspensions can be optimized from two perspectives: improving the adaptability to severe tread wear and suppressing the formation of severe tread wear.

Improved structures and active control systems have been shown to enhance dynamic performance [3–9]. However, due to their numerous components, which result in high costs, reduced reliability, and inconvenient maintenance, they are still in the experimental stages and not widely used in practical engineering applications. Furthermore, research on improving dynamic performance from the perspective of optimizing wheel-rail profiles has been carried out by many scholars [10–14]. Nevertheless, the newly designed wheel-rail profile needs to be evaluated by a long-term line test to prove its performance in all aspects. In this regard, the optimization of conventional passive suspensions can still be considered as an effective solution.

The design optimization of mechanical systems aims to achieve an effective compromise between complex and conflicting design criteria, thereby balancing various indicators and achieving superior performance [15]. Over the past decades, numerous scholars have studied

CONTACT Yuan Yao yyuan8848@163.com State Key Laboratory of Rail Transit Vehicle System, Southwest Jiaotong University, Chengdu, Sichuan, China

the multi-objective optimization of bogie suspensions. Yao and others proposed the concept of robust stability aiming at the hunting motion mode, and optimized the suspension parameters to obtain the suspension parameter matching rules of high-speed trains through the improved non-dominated sorting genetic algorithm NSGA-II [16–19]. Chen and others used genetic algorithms to optimize stability and wear performance of a high-speed train, and revealed the evolution process of wheel wear [20]. Zou and others established the surrogate model of rail vehicles and used genetic algorithms to optimize stability and ride comfort [21].

Although the above research has improved the dynamic performance of high-speed trains, the optimization for high-speed train with severe tread wear is scarce. The optimization of the wear index is mostly the maximum value of wear number without considering the distribution of wear number. Aiming at the wheel hollow wear problem and multi-objective optimization efficiency, a hollow wear index (HWI) is proposed. In this study, we use the multi-objective particle swarm optimization algorithm based on adaptive grid algorithms (AGA-MOPSO) to optimize the suspension parameters. Considering that the dynamic performance between low and high conicities is contradictory [18], the ride comfort index at low-conicity, the stability index at high-conicity and the HWI are taken as the optimization target. Then, four kinds of suspension parameter matching modes are selected in the obtained pareto frontier and the matching rules of suspension parameters are analysed. Finally, the complete hunting motion bifurcation curve is solved to elucidate the nonlinear stability characteristics of the vehicle with different suspension parameter matching.

2. Dynamic modeling

This section introduces a vehicle model established in the simulation software SIMPACK, and presents the wheel-rail geometry.

2.1. Vehicle dynamic modeling

Based on actual dynamic parameters of a high-speed train operating in China, the dynamic model of the vehicle is established in the multi-body dynamics simulation software SIMPACK. As shown in Figure 1, the dynamic model with 62 degrees of freedom consists of 17 rigid

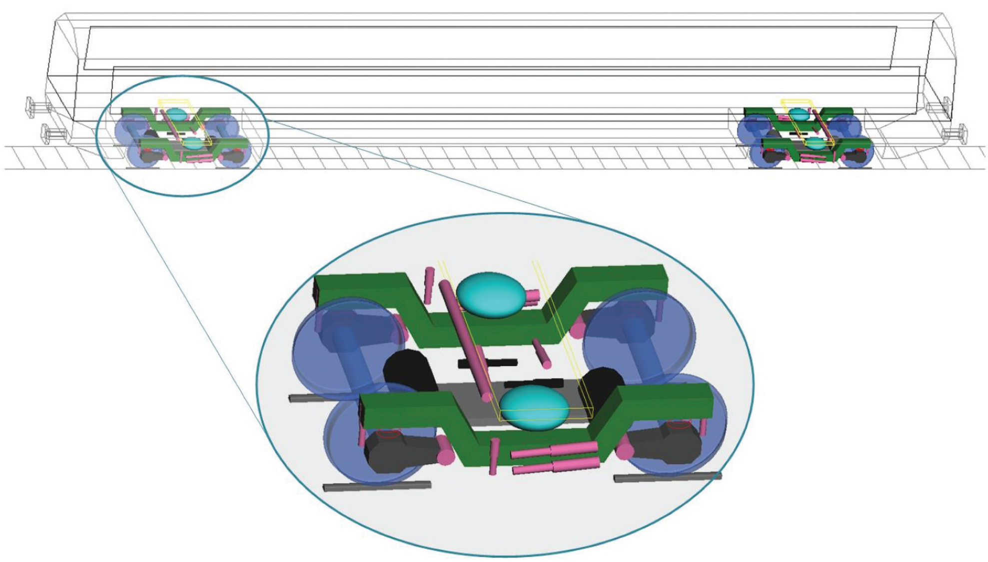

Figure 1. Vehicle dynamic model.

Table 1. Main dynamic parameters.

Name	Value	Unit
Length between bogie centers	17.4	m
Wheel base	2.5	m
Axle load	13	t
Wheel rolling radius	0.46	m
Track gauge	1.435	m

Table 2. The profiles of wheel and rail.

Contact state	Rail	Wheel	Equivalent conicity (3mm)
Low	CN60_M	S1002G_N	0.06
Normal	CN60_S	S1002G_N	0.18
High	CN60_S	S1002G_W	0.41

bodies, including one carbody, two bogie frames, four wheelsets, two mounts with motors and eight axle boxes. The primary suspension of the vehicle acts between the wheelset and bogie frame, consisting of axle box springs, primary vertical dampers and rotating arms. The secondary suspension operates between the bogie frame and carbody, comprising lateral dampers, yaw dampers, vertical dampers, air springs and anti-roll bars. The mount with motors is connected to the frame by bushings, motor bump stops and motor dampers. The dampers are represented by a Maxwell model that connects the stiffness and damping elements in series, and the yaw damper adopts a piecewise linear damping Maxwell model. The nonlinear characteristics of dampers and secondary bump stops are considered. The wheel-rail creep force is calculated by the FASTSIM algorithm [22].

The main parameters of the vehicle are shown in Table 1.

2.2. Wheel-rail contact geometry

Considering the actual operation of high-speed trains, this study focuses on straight line. The track spectrum of Wuhan-Guangzhou high-speed railway is adopted as track irregularities, which represents the overall track irregularity level of Chinese high-speed railway and is widely used in dynamics simulation [23].

Table 2 shows three kinds of wheel-rail geometric contact states that occur during operation period. CN60_M and CN60_S represent measured rail and standard profiles. S1002G_N and S1002G_W represent new and wear wheel profiles. The matching of CN60_M and S1002G_N is employed to simulate low-conicity condition, and CN60_S and S1002G_N is used to simulate normal-conicity condition. The high-conicity condition adopts the profiles of CN60_S and S1002G_W. Figure 2(a) shows the mentioned profiles. Figure 2(b) shows equivalent conicity curves at different wheel-rail contact states solved by the harmonic and quasi-elastic method.

3. Severe tread wear

The vehicle performance can always be satisfactory when the wheel tread is normal, but the occurrence of severe tread wear endangers driving safety. The main form of severe tread wear and HWI are introduced in this section.

3.1. Wheel hollow wear

Due to the frequent occurrence of frame lateral vibration acceleration alarm, the wheelset wear of the alarm bogies on Beijing-Shanghai, Wuhan-Guangzhou and Lanzhou-Xinjiang lines was investigated. It was found that the tread of the alarm bogies had different degrees of wheel hollow wear,

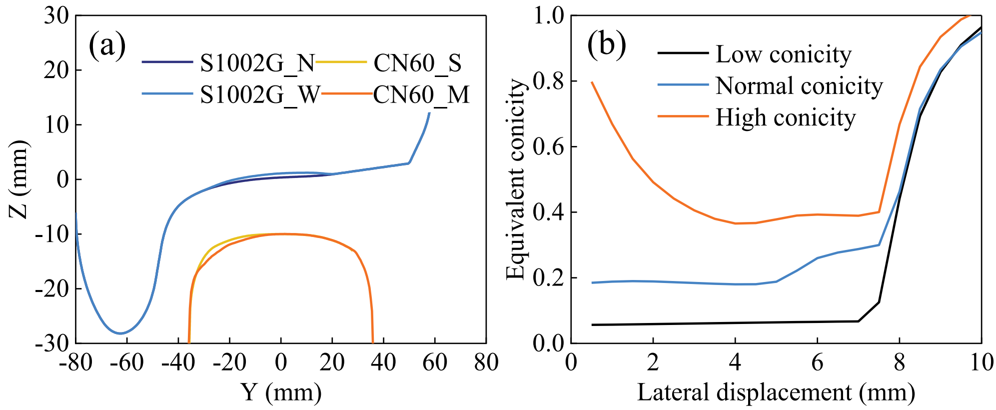

Figure 2. Wheel-rail profiles and contact geometries: (a) wheel-rail profiles; (b) wheel-rail contact equivalent conicity.

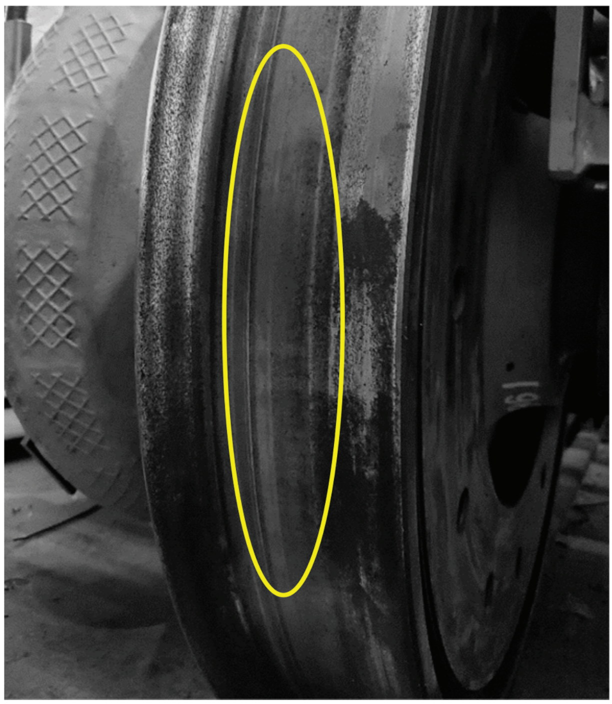

Figure 3. Wheel hollow wear.

and the severe tread wear was mainly concentrated near the rolling circle, forming an obvious groove [24], as shown in Figure 3.

Different from the normal wear of tread, wheel hollow wear often leads to removing a lot of materials during repair, which greatly reduces the service life of wheelsets and increases operating costs. Studies revealed that wheel hollow wear has a significant effect on vehicle dynamics and the rail wear [25,26]. Therefore, the occurrence of wheel hollow wear should be avoided or delayed as much as possible.

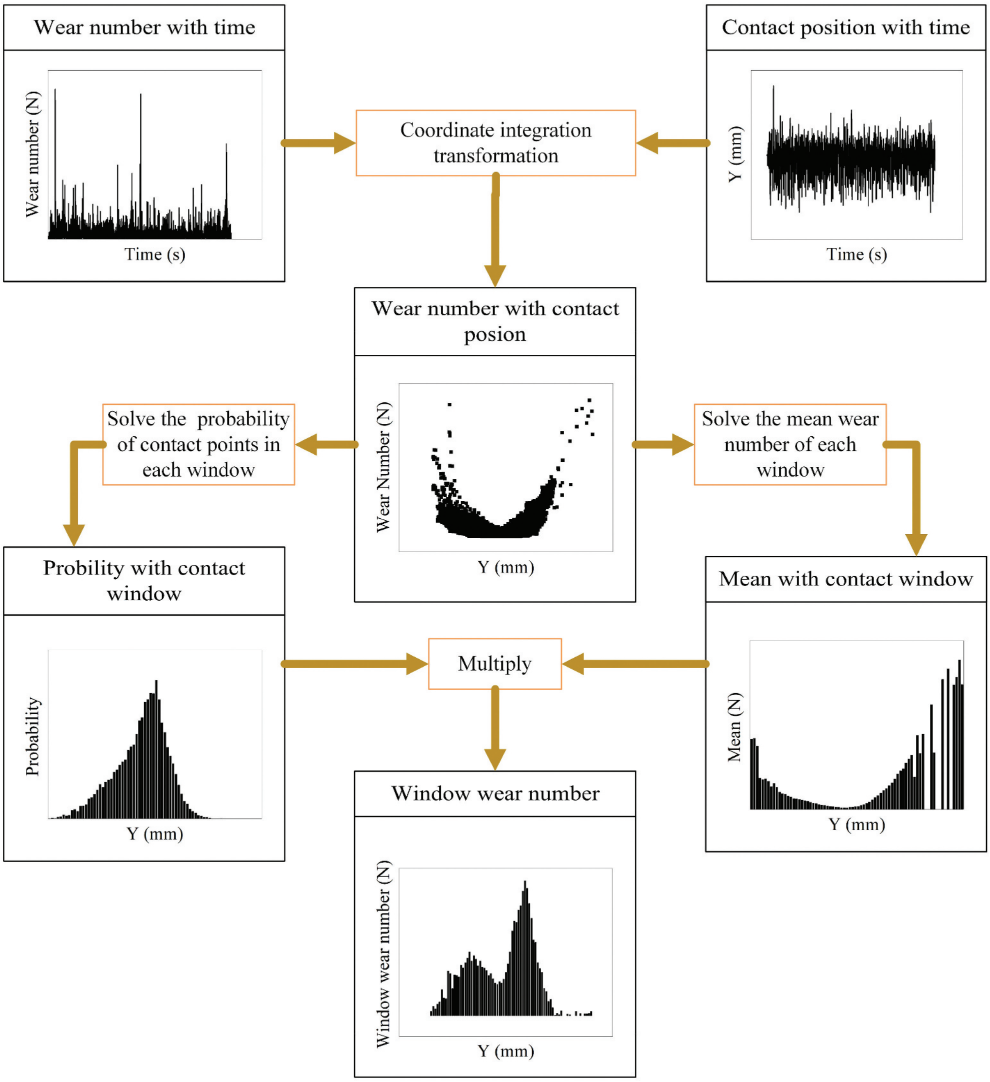

Figure 4. Window wear number solution process.

3.2. Hollow wear index

To reduce the development rate of wheel hollow wear, the HWI is proposed. The solution process of a window wear number used in HWI is shown in Figure 4. For accuracy and efficiency, the track length set in this paper is 5 km. First, the results of wear number and contact position are extracted from simulation, and the relationship between them is obtained by coordinate integration transformation. Second, the position of wheel-rail contact point is divided into windows. Third, the number of contact points in each window is sorted out to calculate occurrence probability of contact points in each window, and the mean wear number of contact points in each window is calculated. Finally, the window wear number is obtained by multiplying the occurrence probability of the contact point of each window with its corresponding mean wear number.

The window wear number characterizes the wear resistance of each window. However, the performance of wheel hollow wear is mainly due to the narrow bandwidth and deep wear. Therefore, the maximum window wear number is divided by the contact bandwidth to obtain

HWI that considers the severity and distribution of wheel wear. In order to avoid the influence of a few abnormal contact points, the probability values of 0.15% and 99.85% are taken for the wheel-rail contact range to calculate the contact bandwidth. The value of the wear number is based on the following formula:

$$T_\gamma = T_x \gamma_x + T_y \gamma_y \tag{1}$$

where T_x and T_y are the transverse and longitudinal creep forces respectively, while γ_x and γ_y are the transverse and longitudinal creep rates. The lateral position of the contact point obtained by simulation is processed by percentage filtering, and the window is divided according to 0.5 mm. The window wear number can be obtained by multiplying the probability of the contact point occurrence with the mean wear number of contact points in each window, as shown below:

$$P(\mathrm{Y}_k) = n_k / N \tag{2}$$

$$T_\gamma(\mathrm{Y}_k) = \sum\nolimits_{i=1}^{n_k} T_{\gamma i} / n_k \tag{3}$$

$$\mathrm{WWN}(\mathrm{Y}_k) = P(\mathrm{Y}_k) T_\gamma(\mathrm{Y}_k) \tag{4}$$

where Y_k represents the kth window divided. N is the simulation sample number, and n_k is the number of contact points in the kth window. $P(\mathrm{Y}_k)$ is the probability of the contact point occurrence in the kth window. $T_{\gamma i}$ is the wear number of ith contact point, and $T_\gamma(\mathrm{Y}_k)$ is the mean wear number of the contact points in the kth window. $\mathrm{WWN}(\mathrm{Y}_k)$ is the window wear number of the kth window. The definition of HWI is as follows:

$$\mathrm{HWI} = \mathrm{WWN}(\mathrm{Y})_{\max} / (\mathrm{Y}_{\max} - \mathrm{Y}_{\min}) \tag{5}$$

where ($\mathrm{Y}_{\max}$-$\mathrm{Y}_{\min}$) indicates the bandwidth of contact points.

Since the influence of contact patches' shape is not considered, HWI can only reduce the development rate of wheel hollow wear, and cannot accurately describe the wheel hollow wear across various phases. However, considering the computational efficiency, this is a compromise that has to be made for multi-objective optimization problem.

4. Suspension parameter optimization

This section introduces the process of suspension parameter optimization. Initially, three indicators are determined as optimization objectives. Subsequently, the main suspension parameters and constraints are given. Ultimately, the optimization of suspension parameters is realized by means of MATLAB-SIMPACK co-simulation.

4.1. Optimization objectives

To improve the efficiency of multi-objective optimization problems, it is a feasible method to determine the optimal dynamic index under extreme wheel-rail contact conicities because the dynamic index can always be satisfactory under normal condition. Considering the contradiction between indicators, three dynamics indexes corresponding to different wheel-rail contact states are selected for evaluation, namely, the ride comfort of low-conicity, the stability index of high-conicity and the HWI at normal-conicity. Wheel-rail contact states are detailed in Table 2 and Figure 2.

The Sperling index W is an internationally recognized method to evaluate vehicle ride comfort, which is defined as follows:

$$W = 3.57 \sqrt[10]{\frac{A^3}{f} F(f)} \tag{6}$$

where A represents the acceleration frequency domain amplitude obtained by time-frequency conversion of the measured car body acceleration, f denotes the corresponding frequency, and $F(f)$ is the frequency correction coefficient. Since the excessive lateral ride comfort is prone to occur in the low-conicity condition, this study selects the lateral ride comfort index under the low-conicity condition as the optimization target, which is recorded as W_{low}.

The evaluation index of stability is judged by the lateral acceleration of the bogie frame. According to the provisions of GB/T5599–2019 [27], the corresponding frame position above the axle box is set as the acceleration measuring point. The sampling frequency is 400 Hz, and the measured acceleration data is filtered by a band-pass filter with a bandwidth being 0.5 ~ 10 Hz. In this study, the maximum frame acceleration after the removal of outliers is taken as the stability index. When the tread wear is serious, resulting in an increase in the wheel-rail contact conicity, or even a negative slope, the stability will deteriorate. Therefore, the stability of high-conicity condition is selected as the optimization objective, expressed by A_{high}.

For the optimization of the severe tread wear, the HWI at normal-conicity is selected for the purpose of effectively suppressing the formation of wheel hollow wear.

The optimization indexes are shown in Table 3.

4.1.1. Design parameters and constraint

The selection of design variables is an important part of multi-objective optimization problems. Too few design variables may lead to unsatisfactory optimization results, while too many design variables will reduce optimization efficiency and the feasibility of optimization schemes. Based on years of research experience in vehicle system dynamics within our team [16–20], the main design variables are determined as longitudinal primary stiffness (*kpy*), damping of the yaw damper (*csx*), damping of the secondary damper (*csy*) and series stiffness of the yaw damper (*kncsx*). The unloading force of yaw dampers is maintained at 10 kN, and the unloading speed is changed to realize different values of *csx*. The optimized parameter range selected is shown in Table 4.

The series stiffness of yaw damper mentioned in this study is the series stiffness of damper mounting seats, rubber joints stiffness and oil stiffness, as follows:

$$kncsx = \frac{k_s k_j k_o}{2k_j k_o + 2k_s k_o + k_j k_s} \tag{7}$$

Table 3. Optimization indexes for multi-objective optimization.

Index	Calculation condition		Description
	Speed (km/h)	Conicity	
W_{low}	200	0.06	Lateral ride comfort at low-conicity
A_{high}	350	0.41	Bogie frame acceleration at high-conicity
HWI	300	0.18	Hollow wear index

Table 4. Design variables and optimization ranges.

Parameter	Design range	Description
kpx	10–120 (kN/mm)	Longitudinal primary stiffness
csx	200–2500 (kN·s/m)	Damping of yaw damper
csy	10–70 (kN·s/m)	Damping of lateral secondary damper
kncsx	5–15 (kN/mm)	Series stiffness of yaw damper

where k_s represents the rubber joint stiffness, k_j denotes the damper mounting seat and k_o represents oil stiffness. Generally, the series stiffness is close to the optimization value by adjusting the rubber joint stiffness of the damper. The rubber joint stiffness can be obtained by Equation (8).

$$k_j = \frac{2kncsxk_s k_o}{kncsxk_o - 2kncsxk_o - kncsxk_s} \tag{8}$$

By referring to literature [28] and combining with engineering experience, the optimization range of series stiffness of yaw damper is given.

To ensure the curving performance of the vehicle, a severe operational scenario on curved tracks is set to a curve with a radius of 5000 m and cant deficiency of 110 mm [20]. The derailment coefficient, sum of wheelset lateral forces, and wheel unloading rate are checked according to GB/T5599–2019 [26], whose limits are 0.8, 58 kN and 0.8.

4.2. Multi-objective optimization problem description

Multi-objective optimization problems typically have a solution set called Pareto optimal solution, and its image in the objective function space is called Pareto front. Under the premise that dynamic index does not exceed the constraints, we try to adjust the suspension parameters mentioned in Table 4 within a given range of values to minimize the objective functions defined in Table 3 for the optimization problem in this study. The multi-objective optimal design problem is stated as:

$$min\{W_{low}, A_{high}, HWI\} \tag{9}$$

In multi-objective optimization problems, common optimization algorithms include particle swarm optimization (PSO) and genetic algorithm (GA). We consider the above two algorithms in optimization, and finds that PSO can find the optimal result faster under the same computing power. Although the final optimization results of this study incorporate two optimization algorithms, we recommend using particle swarm optimization algorithm for future selections of optimization algorithms. PSO is an evolutionary computation technique that originates from research on the foraging behaviour of birds. Each member of the block randomly adjusts the search direction by learning from its own experience and the experience of other members, causing the movement of the flock to transition from disorder to order, and ultimately achieving the optimal solution. Since conventional PSO algorithms fail to fully consider particle density information in the global optimal particle set and the balance between global and local search capabilities, AGA-MOPSO is adopted. A detailed description of AGA-MOPSO is given in reference [29].

The optimization of vehicle suspension parameters has three processes. First, optimization objectives based on the problems manifested in the operation are chosen. Second, the corresponding suspension parameters as optimization objects according to the optimization objectives are selected. Finally, the multi-objective optimization with the help of optimization algorithms and simulation software is achieved. Figure 5 shows the implementation flow of a multi-objective optimization problem.

It can be seen from Figure 5 that the multi-objective optimization problem described in this study mainly uses SIMPACK and MATLAB. First, three optimization indexes are formulated according to problems shown in the operation of existing vehicles. Second, a dynamic model is established in SIMPACK, and a corresponding file.spf is established according to the optimization indexes. Third, the PSO algorithm is applied by MATLAB software, which is used to determine the value of the suspension parameters. A pre-processing language.sjs of SIMPACK is called by MATLAB to realize modification and integral calculation of the model. Finally, the language.qs and file.spf of the post-processing module are called to obtain the value of the optimization index after the result file is obtained. The value of the optimization index is returned to the PSO algorithm to provide the basis for the next suspension parameter value until cyclic condition is satisfied.

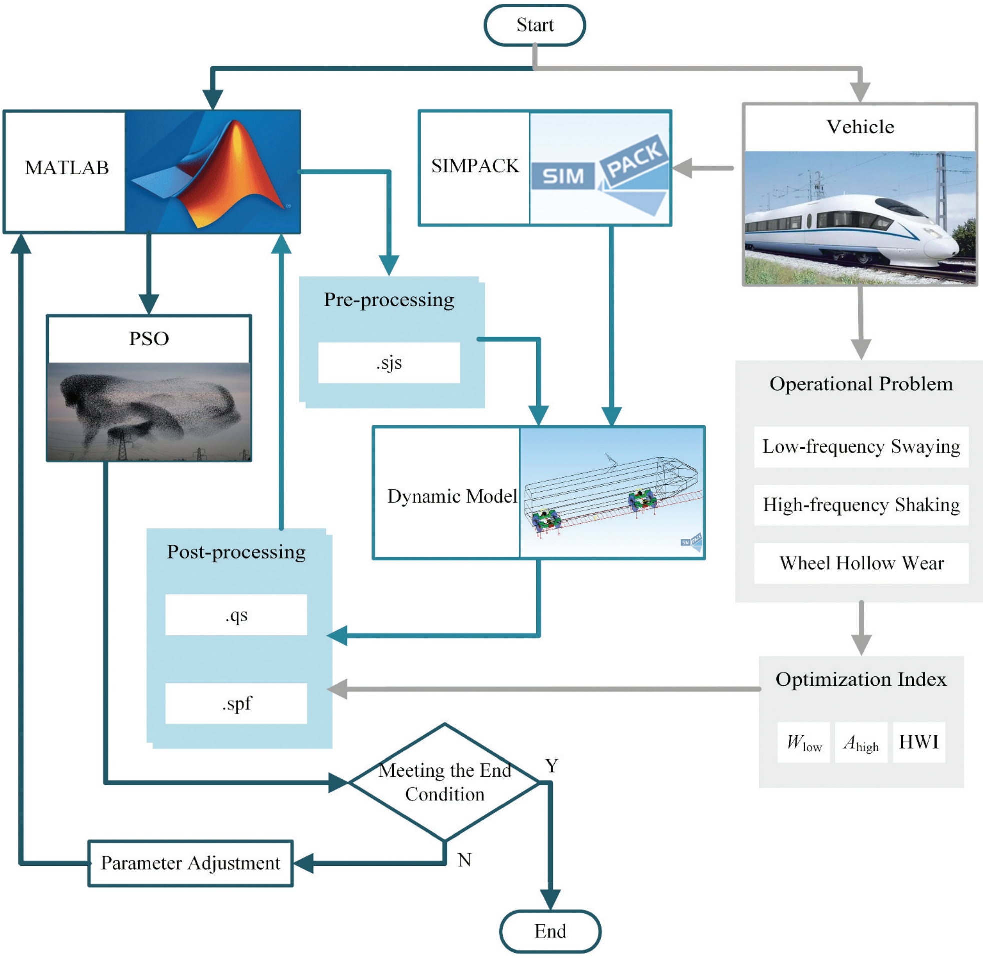

Figure 5. Implementation flow of the multi-objective optimization problem.

5. Results and discussion

This section gives the Pareto front of multi-objective optimization, and selects four clusters in the Pareto front according to different optimization focuses. The correlation between suspension parameters and optimization objectives is analysed using the Pearson coefficient. Then, four types of models are established corresponding to the centre points of the four clusters. Finally, in order to evaluate the reliability of the optimization scheme more comprehensively, the dynamic performance under three wheel-rail contact states and hunting stability are analysed.

5.1. Pareto front and parameter matching analysis

Pareto front was obtained through the multi-objective optimization method described in the previous section, as shown in Figure 6. The horizontal coordinate and vertical coordinate respectively represent the W_{low} and A_{high}. In addition, the colour of the data point represents the HWI, and the darker colour means the better wear performance. To analyse the matching rules of suspension parameters, four representative clusters, labelled as A, B, C, and D, are selected in pareto frontier, as marked in Figure 6. Cluster A has the lowest

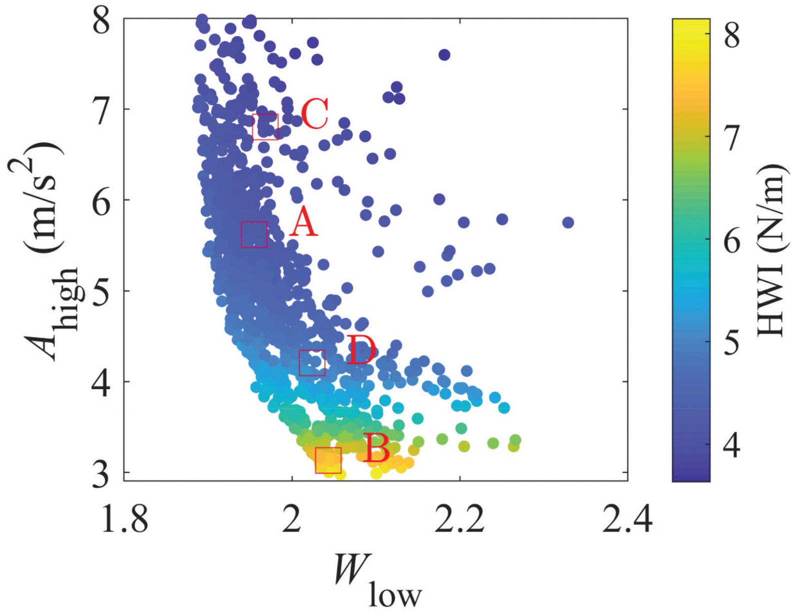

Figure 6. Pareto frontier of multi-objective optimization.

W_{low}, Cluster B has the lowest A_{high}, and Cluster C corresponds to the best HWI. Cluster D represents a trade-off among all optimization objectives, resulting in more balanced performance.

Figure 7 displays the distribution of suspension parameters of the four clusters in the form of boxplot. Matching rules of the suspension parameters can be summarized by analysing parameter distribution under different focuses on the optimization objectives. It can be drawn from Figure 7 that the parameter distributions of the four clusters differ slightly with respect to *csy*. Cluster A adopts a lower *kpx*, *csx*, *csy* and *kncsx*. For Cluster B, the parameter combination of a higher *kpx* and *csx* as well as a higher *csy* and *kncsx* is adopted. Cluster C aims to minimize both *kpx* and *kncsx* to maintain superior wear performance. The dynamic performances of Cluster D are more comprehensive, which has *csx* close to Cluster A and *csy* close to Cluster B. Moreover, the distribution of *kpx* and *kncsx* in Cluster D is divided into two categories: the first exhibits a higher value of *kpx* alongside a lower value of *kncsx*, while the second demonstrates the opposite trend with a lower *kpx* and a higher *kncsx*.

The three dynamic indexes are affected by hunting motion which is a coupling motion of lateral and yaw motion. The energy of the hunting motion is dissipated mainly by lateral and yaw damping which are provided by lateral and yaw damper. To better analyse the correlation between indexes and suspension parameters, the ratio of yaw damping to lateral damping is defined as *RYL*, and the stiffness of *kpx* and *kncsx* in series is defined as *YS*. The *RYL* and *YS* can be obtained by

$$RYL = \frac{2m \cdot csx + n \cdot csy}{csy} \tag{10}$$

$$YS = \frac{kpx \cdot kncsx}{kpx + kncsx} \tag{11}$$

where, *m* represents the lateral distance from the connection point of the yaw damper to the centre of the carbody, and *n* represents the longitudinal distance from the connection point of the lateral damper to the centre of the carbody.

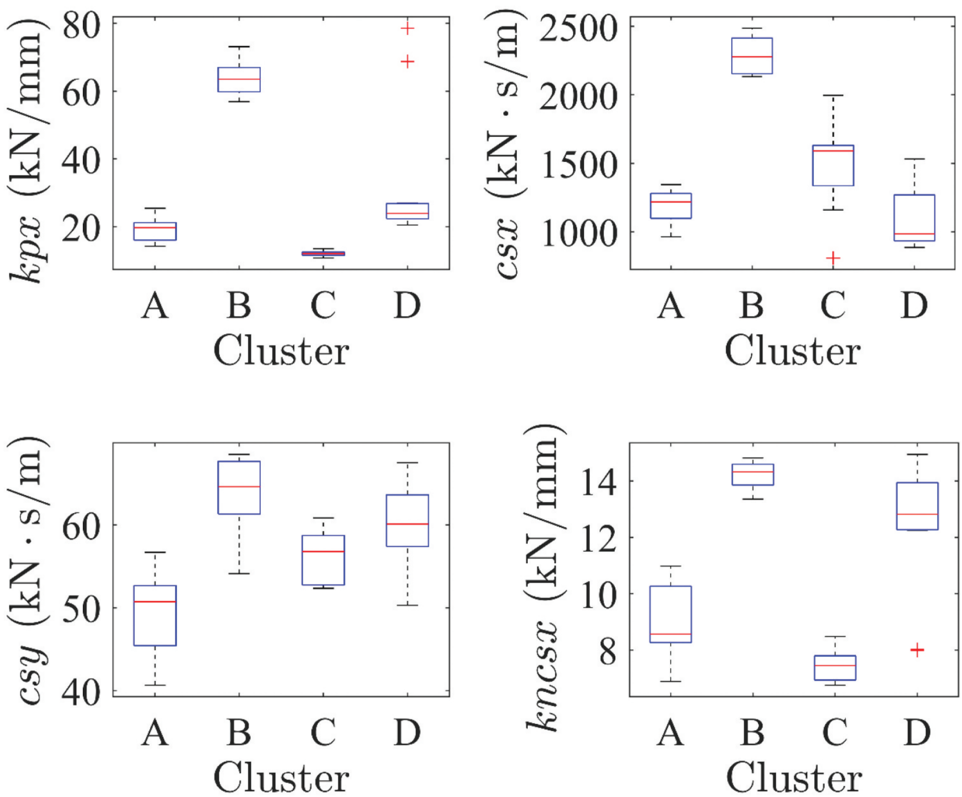

Figure 7. Suspension parameter distribution of four clusters.

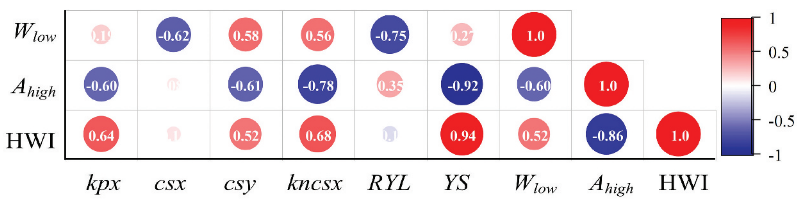

Figure 8. Person correlation coefficient between suspension parameters and optimization indexes.

The Pearson coefficient is used to quantitatively describe the correlation between suspension parameters and optimization indexes, as shown in Figure 8.

In Figure 8, the value range is -1 to $+1$, corresponding to completely negative correlation and completely positive correlation respectively. The W_{low} and RYL have a strong negative correlation, which means the larger the value of RYL, the lower the value of W_{low}. When the W_{low} cannot meet the requirements, increasing the RYL value will make sense. In order to obtain a lower value of A_{high}, it is necessary to increase the value of YS, for A_{high} has a strong negative correlation with YS. A strong contradiction between the HWI and A_{high} can be found in Figure 8, and the HWI also shows a strong positive correlation with YS. To achieve better wear performance and ensure operation economy, reduce the value of YS as much as possible on the premise of ensuring stability is necessary.

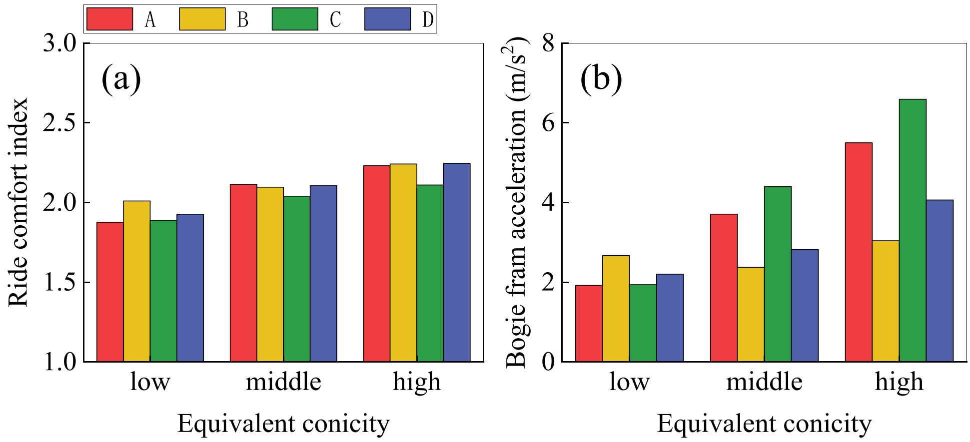

Figure 9. Dynamic performance at different conicities: (a) ride comfort; (b) bogie frame acceleration.

5.2. Evaluation of optimization schemes

In order to increase optimization efficiency, only ride comfort at low-conicity and stability at high-conicity are considered when selecting the optimization index. It is necessary to calculate the ride comfort and stability of the four clusters under three wheel-rail contact states for a reliability evaluation. The suspension parameters of each cluster correspond to the centre point selected in the Pareto front of Figure 6. The models A, B, C, D are used to represent the parameter combination corresponding to clusters A, B, C, D, respectively. The calculation results are displayed in Figure 9.

It can be seen from Figure 9 that the ride comfort of the four models at normal-conicity and high-conicity still meets the requirements. The stability of models A and C rapidly decreases with the increase of conicity, while model D exhibits a slower decrease. The stability of model B is not affected by changes in conicity, which has good conicity robustness. The ride comfort and stability indexes under three wheel-rail contact states can meet the requirements, and the optimization results are reliable.

The HWI quantifies the quality of wear performance for a giving scheme, which can simply and efficiently reflect the wear performance of high-speed trains. Figure 10 gives the window wear number about four models to display wear number distribution characteristics.

In Figure 10, the wear performance of model B is the worst, which is mainly manifested by the high window wear number, and the wear is not uniform. The wear performance of model C is the best, with only 25% less contact bandwidth than the widest model B, but the maximum value of its window wear number is reduced by 47%, and the wear is more uniform. The wear performance of models A and D is relatively close. Model D that makes a trade-off design can be given priority for engineering application. If the wear problem is less of a concern than stability, Model B is also a good design solution, for it has a good conicity robustness.

5.3. Hunting stability analysis

The acceleration of the bogie frame is easily measurable and commonly serves as an index for evaluating stability during the operation of high-speed trains. However, the stability of high-speed trains is determined by the stability of the hunting motion from the perspective of vehicle system dynamics. The hunting motion is a kind of self-excited vibration whose input energy comes from kinetic energy and driving force, and the energy of the hunting motion increases with the speed. When the energy dissipated by the system is less than the increased energy, the stability of the

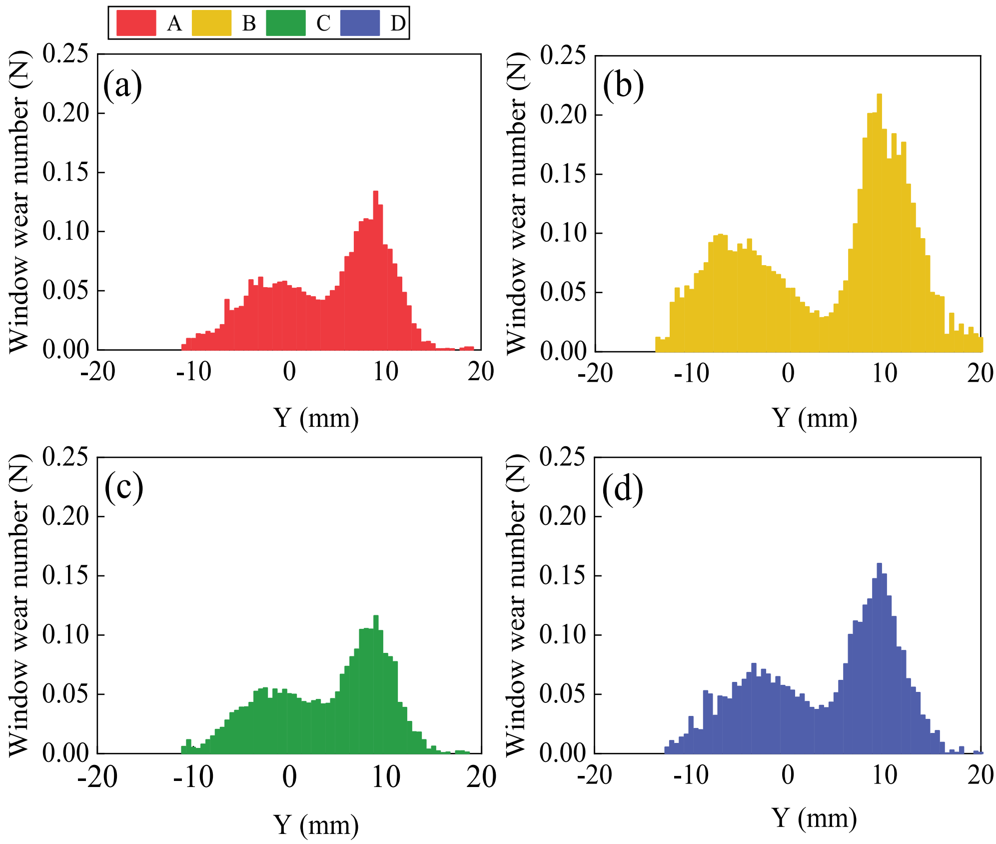

Figure 10. Window wear number about four models: (a) model A; (b) model B; (c) model C; (d) model D.

hunting motion decreases. This section analyses the dynamic performance of the four models from the perspective of hunting stability.

5.3.1. Linear stability analysis

Linear stability is applicable to the study of regional stability near the equilibrium point of a linear system, where all nonlinearities contained in the suspension elements and wheel-rail contact are linearized. The common linear stability analysis method is root loci method, which is analysing the relationship between the eigenvalues of Jacobian matrix and the speed of vehicle system. When the real part of the eigenvalues corresponding to the hunting motion mode passes through imaginary axis, the system is unstable. The damping ratio ζ and damped vibration frequency f of modes are defined as the following equations:

$$\eta = a + bi \tag{12}$$

$$f = \frac{|b|}{2\pi} \tag{13}$$

$$\zeta = \frac{a}{\sqrt{a^2 + b^2}} \tag{14}$$

where i denotes the imaginary unit, η represents the eigenvalue of the linear system, a and b are its real part and imaginary part, respectively. In this study, a negative value of a indicates that the modal vibration will be dampened, so the smaller the value of ζ is, the better the lateral stability is.

The root loci of the vehicle system with variation in velocity according to four models are shown in Figure 11, the horizontal axis represents the mode damping ratio ζ, and the vertical axis represents the damped vibration frequency of mode. Each root loci is composed of 17 sets of eigenvalues with the speed varying from 100 to 900 km/h, and each '+' indicates a corresponding mode. The larger symbol represents a larger running speed. The hunting motion modes mainly include the primary hunting motion dominated by the hunting energy of carbody and the secondary hunting motion dominated by the hunting energy of bogie. The hunting motion with a larger damping ratio at the same speed is selected as the threatening hunting motion mode, referred to as THMM, which is highlighted. As shown in Figure 11, with the speed increases, THMM may shift from a primary hunting to a secondary hunting. VJ is defined as the velocity jump about THMM. Table 5 shows the VJ for four models under different wheel-rail contacts. THMM can be used to explain why the ride comfort and stability in Figure 9 are contradictory in some conditions. The primary hunting affects ride comfort, while secondary hunting affects stability. If the THMM of the model is primary hunting, then the ride comfort and stability agree with the THMM damping ratio, as the stability is affected by the amplitude of bogie frame

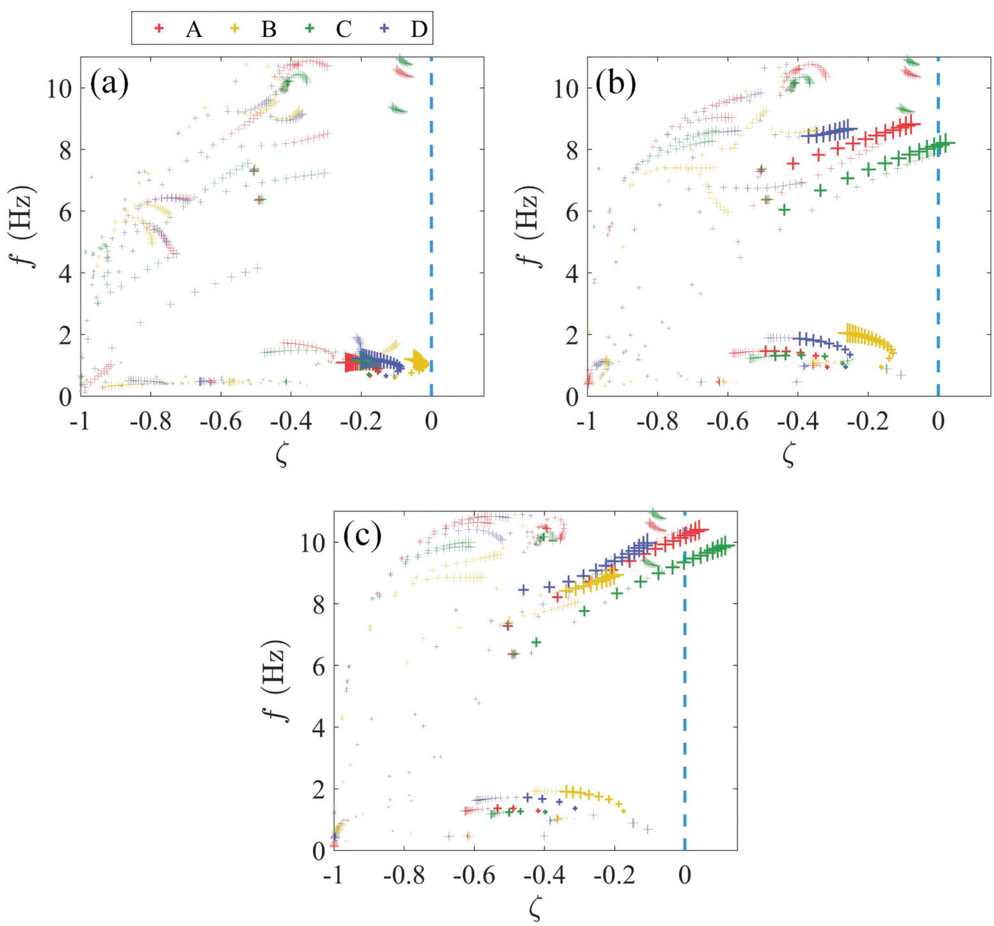

Figure 11. Root loci of the vehicle system with variation in velocity under different wheel rail contacts: (a) low-conicity; (b) normal-conicity; (c) high-conicity.

Table 5. Velocity jump values for four models under different wheel-rail contacts.

Model	VJ (km/h)		
	Low-conicity	Normal-conicity	High-conicity
A	>900	350	150
B	>900	>900	450
C	>900	300	150
D	>900	500	250

acceleration. However, the ride comfort is related to the frequency correction coefficient $F(f)$ in Equation (6), and the low-frequency correction coefficient is larger than the correction coefficient at high frequencies. When the THMM of the model is secondary hunting, the stability will conflict with the ride comfort and be compatible with the THMM damping ratio. The THMM of four models is characterized by primary hunting motion under the low-conicity condition, so the ride comfort and stability are not contradictory. Model B has the best stability and worst ride comfort under the high-conicity condition, while Model C has the best ride comfort and worst stability. It is due to that when the velocity is 350 km/h, the THMM of Model B is primary hunting and the THMM of Model C is secondary hunting.

Through the root loci diagram under three wheel-rail contact states, it is easy to find that with the increase of equivalent conicity, THMM has a tendency to develop from primary hunting to secondary hunting. Under the low-conicity condition, the damping ratio of THMM increases first and then decreases as the increase of speed, so the lack of ride comfort mainly occurs at low speed under the low-conicity condition. In the normal-conicity condition, the THMM of models B and D shows primary hunting motion at a speed of less than 500 km/h, so the frame acceleration of both models B and D is small. Under the high-conicity condition, the THMM of Model B jumps when the speed is greater than 450 km/h, while the VJ of the other three models remain below 300 km/h. Therefore, the acceleration level of the frame of Model B is similar to that observed under the low-conicity condition whose THMM is primary hunting at a speed of 350 km/h.

5.3.2. Nonlinear stability analysis

In the linearization process, the 3-mm position of the wheelset along the wheel-rail contact conicity curve is taken as the equivalent conicity, meanwhile, the unloading characteristics of damper and nonlinear characteristics of wheel-rail contact are ignored. It can be seen from Figure 2(b) that the wheel-rail contact conicity changes with the lateral displacement of the wheelset. The energy of the hunting motion will increase as the running speed increases, and the yaw damper is easier to reach the unloading condition. Therefore, it is necessary to conduct nonlinear stability analysis.

In this study, the constant speed method is used to calculate the critical speed. The constant speed method causes the vehicle system to traverse the track irregularity spectrum, which is 200 m in length, at a certain speed before running on a smooth line. Subsequently, observe whether the lateral displacement of the wheelset converges and judge whether the system is stable. The track irregularity spectrum is selected from the AAR5 spectrum, and the simulation time is set to 20 seconds. Due to the significant impact yaw dampers have on stability, the yaw damper fault condition is also considered. As a supplement, the vehicle has eight yaw dampers, and the yaw damper fault condition is the failure of one yaw damper. The lateral displacement of wheelset is the value after 12 seconds. The wheelset lateral displacement of four models under three wheel-rail contact states are obtained and shown in Figure 12.

In Figure 12, the peak value of system's dissipated energy decreases under yaw damper fault condition, and the lower speed can reach the peak value of dissipated energy, so the critical speed decreases. Despite having the best high-conicity stability, the critical speed of model B is greatly reduced under yaw damper fault condition.

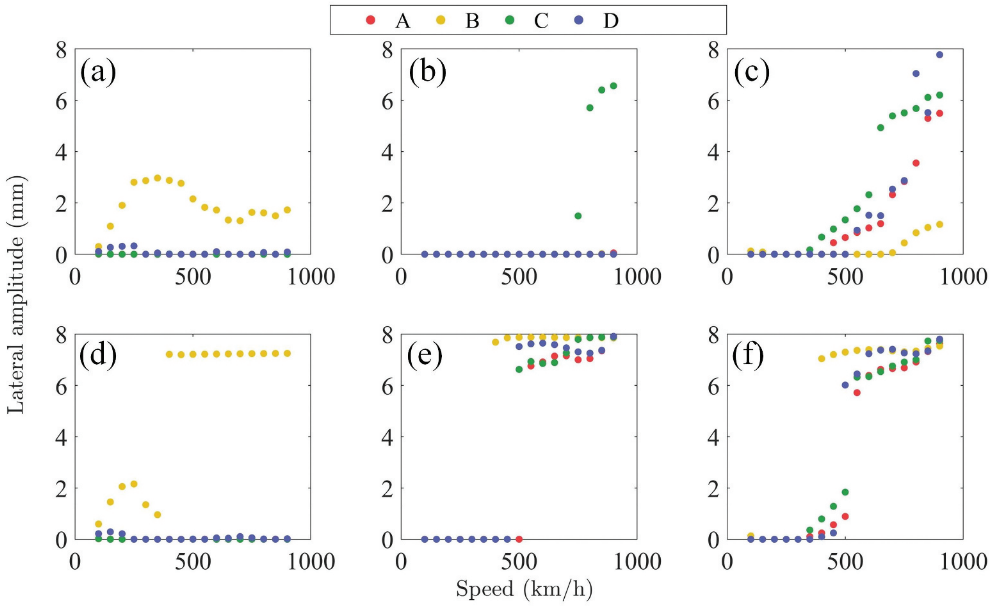

Figure 12. Wheelset lateral displacement of four models under three wheel-rail contact states: (a) low-conicity; (b) normal-conicity; (c) high-conicity; (d) low-conicity with fault yaw damper; (e) normal-conicity with fault yaw damper; (f) high-conicity with fault yaw damper.

5.3.3. Hunting bifurcation analysis

The initial state of the vehicle system determines whether the hunting motion will converge, so different track excitations correspond to different critical speeds. The bifurcation diagram of hunting motion can explain the convergence and divergence conditions of the hunting motion at different speeds. It can be seen from Figure 12(a–c) that the critical speed is very high, and there is no problem of insufficient stability. However, when the yaw damper fails, the critical speed decreases obviously, especially model B, so drawing a hunting motion bifurcation curve for further evaluation is necessary. The bifurcation diagram of hunting motion includes balance points, stable limit cycles and unstable limit cycles. The unstable limit cycle, which exists between the stable limit cycle and the balance point, divides the attraction domain of both the divergence and convergence of hunting motion. In order to facilitate expression, the stable limit cycle with an amplitude less than 3 mm is uniformly identified as a balance point. The bifurcation of hunting motion is divided into supercritical bifurcation and subcritical bifurcation. The supercritical bifurcation means that the linear critical speed is equal to the nonlinear critical speed. Conversely, when the nonlinear critical speed is less than the linear critical speed, it is referred to as subcritical bifurcation [30].

Initial state excitation method (ISEM) is an effective method for solving complete hunting motion bifurcation curve. The quasi-periodic solution is weighted and adjusted to serve as the initial state of the system. Subsequently, the motion state of the rigid body is obtained through time domain integration along a smooth track. The principle for selecting the time of quasi-periodic solution is to identify the moment when the lateral movement of the wheelset is minimal. The adaptive solver SODASRT2 with the initial step size of 10^{-12} is chosen in SIMPACK. In the velocity interval where the unstable limit cycle exists, there must exist two adjacent initial states that make the system converge and diverge after several periodic motions, as shown in Figure 13(a,b). In Figure 13(c), the green hollow points represent the unstable limit cycle, and the values are based on the periodic solution observed during the initial stage of divergence and convergence. The red solid point and the blue solid point represent the stable limit cycle and balance point, respectively, corresponding to the amplitudes of divergence and convergence [31].

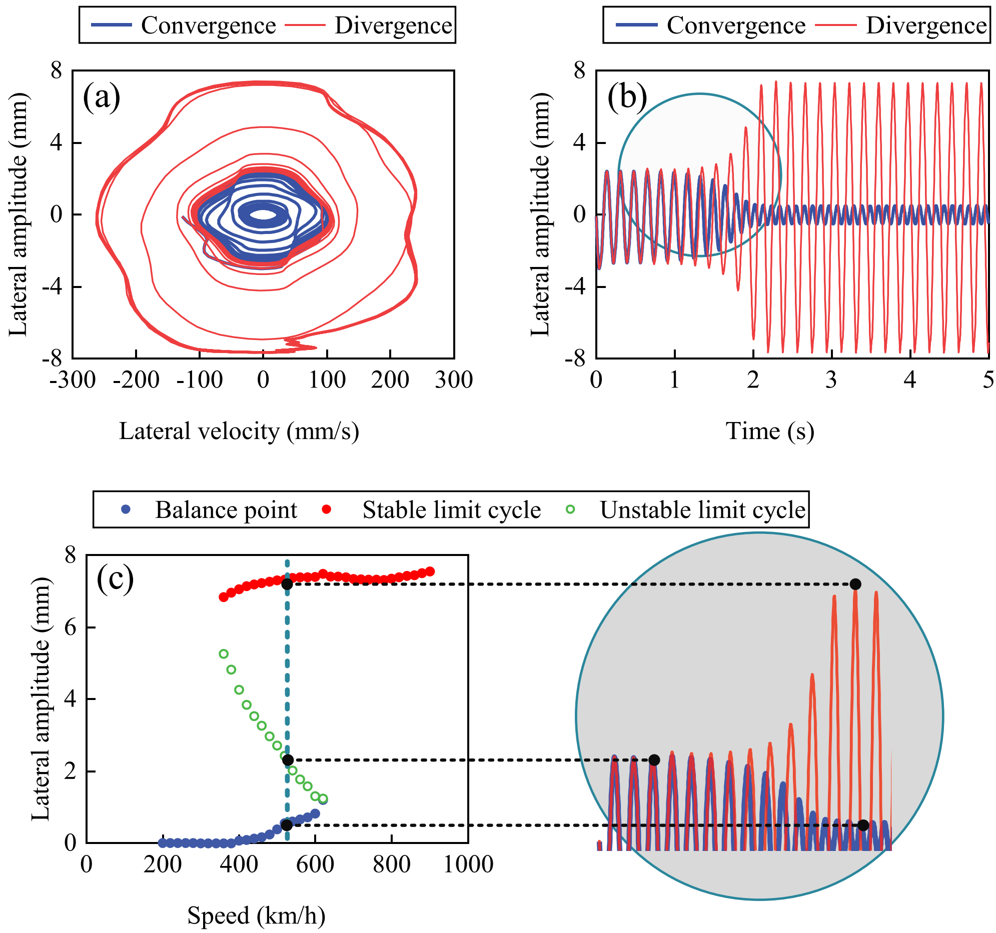

Figure 13. Hunting bifurcation solution based on initial state excitation method: (a) phase diagram; (b) time domain result; (c) hunting bifurcation.

The low-conicity condition only appears in some special sections, and the yaw damper fault is a small probability event, so the normal-conicity and high-conicity working conditions with the fault yaw damper are selected due to their lower critical speed, as shown in Figures 14 and 15.

It can be seen from Figure 14 that when the yaw damper fault occurs, the four models are subcritical bifurcation under normal-conicity condition. The small limit cycle solution appears at a lower speed in model C, and the existence of small limit cycles helps the distribution of contact points to be more uniform, which may explain why the wear performance of model C is the best among the four models. The linear stability of models B and D is better from Figure 11(b), and the unstable limit cycle still exists when the speed reaches 900 km/h. The amplitude of the unstable limit cycle is always greater than 3 mm, which means that when the line condition is good, the critical speed of the two models can still be greater than 900 km/h despite the yaw damper fault occurring. As a supplement, the degree of good line condition mentioned here refers to the initial lateral displacement amplitude of the wheelset being within 3 mm when line irregularity is removed. From the change trend of the unstable limit cycle with speed, it is easy to find that the unstable limit cycles of models A and C initially decrease slowly but then rapidly with the increase of speed, while the unstable limit cycles of models B and D initially decrease rapidly but then slowly. Therefore, when the speed is relatively low, the

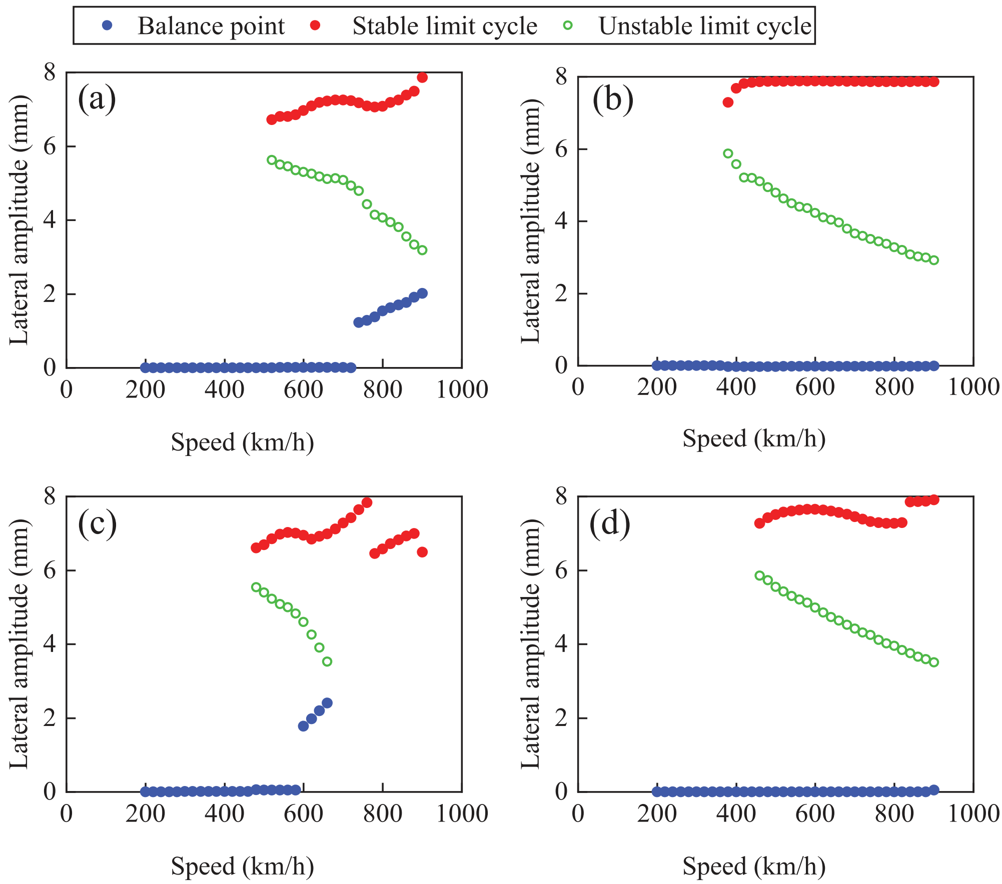

Figure 14. Hunting motion bifurcation curve with fault yaw damper at normal-conicity: (a) model A; (b) model B; (c) model C; (d) model D.

sensibility of models A and C to the track excitation is stronger than that of models B and D. When the speed is relatively high, compared with models A and C, the sensibility of models B and D to the track excitation is higher.

From Figure 15, models B and D are still subcritical bifurcation, while supercritical bifurcation occurs in models A and C under high-conicity condition. Taking model B as an example, when the speed is less than 520 km/h, the lateral displacement of the wheelset is less than 0.5 mm, but when the speed is greater than 620 km/h, there is a risk of sudden increase in the amplitude of the limit cycle. The chaotic solution of model D occurs when the speed is greater than 700 km/h. The amplitude of the unstable limit cycle becomes sensitive to velocity because of high-conicity. The range of unstable limit cycle of model B is the largest, between 1 mm and 6 mm, which indicates that the critical speed gap of model B under different track excitations is large.

6. Conclusions

In this study, the multi-objective optimization of suspension parameters of a high-speed train with severe tread wear has been investigated by multi-objective particle swarm optimization algorithm based on adaptive grid algorithms (AGA-MOPSO). The ride comfort index at low-conicity W_{low}, the stability index at high-conicity A_{high} and the hollow wear index (HWI) at normal-conicity are defined as the optimization objective.

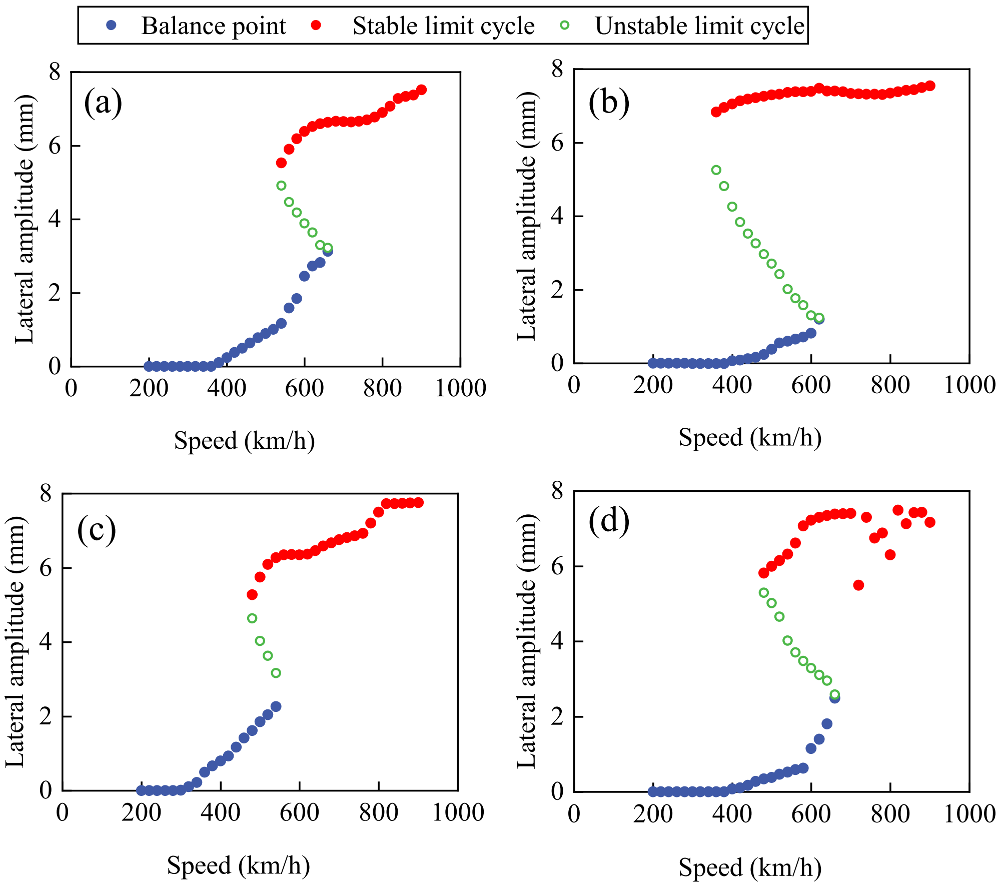

Figure 15. Hunting motion bifurcation curve with fault yaw damper at high-conicity: (a) model A; (b) model B; (c) model C; (d) model D.

(1) The window wear number considers the severity and distribution of wheel wear is proposed. The contact regions in the wheel profile are divided into multiple windows, and the contact point occurrence probability of each window is counted. The product of mean wear number and the occurrence probability of each window is defined as the window wear number. The maximum window wear number is divided by the contact bandwidth to obtain HWI, which can characterize the wear performance more concisely than the wear simulation and more comprehensively than wear number.

(2) For the Pareto front, four types of key suspension parameter combinations referring to different dynamic performances are extracted to summarize parameter matching principles. A smaller *kpx*, *csx*, *csy* and *kncsx* is beneficial to W_{low}; A better A_{high} needs a larger *kpx*, *csx*, *csy* and kncsx; A smaller *kpx*, *kncsx*, median *csy* and *csx* contribute to better HWI; A smaller *kpx*, *csx*, larger *csy* and *kncsx* is beneficial for the trade-off between the three indexes. Two variables, *RYL* and *YS*, are defined to explore the parameter matching principles. The results of Pearson correlation coefficient analysis demonstrate that the *RYL* and *YS* are significantly correlated with W_{low}, A_{high} and HWI. The higher the value of *RYL*, the better the W_{low}. A higher value of *YS* is helpful for the A_{high}. To improve HWI, the value of *YS* needs to be reduced. The HWI exhibits a positive correlation with W_{low} and a negative correlation with A_{high}. The wear index should be as optimal as possible to achieve better economic performance while ensuring the vehicle stability under the condition of high-conicity.

(3) The linear and nonlinear hunting stability of four types of parameter combinations for the vehicle under three wheel-rail contact states is analysed. The root loci method is used to explain why stability and ride comfort sometimes contradict each other. The wheelset hunting bifurcation diagram of the nonlinear vehicle dynamics model established by SIMPACK is obtained by the initial state excitation method (ISEM). The vehicle hunting exhibits subcritical bifurcation under the conditions of low and normal-conicity. The model with better HWI is easy to form supercritical bifurcation, which has small limit cycles at low speeds, especially under the condition of high-conicity. Despite having a high stability margin and good conicity robustness, the critical speed of the model with the best A_{high} is greatly reduced if one of the yaw dampers fails, which deserves attention in further research.

Disclosure statement

No potential conflict of interest was reported by the author(s).

Funding

This work was supported by the National Natural Science Foundation of China [grant numbers 52372403, U2268211], the Natural Science Foundation of Sichuan Province [grant numbers 2022NSFSC0034, 2022NSFSC1901], and the National Railway Group Science and Technology Program [grant number N2023J071].

ORCID

Hu Li http://orcid.org/0009-0008-5455-016X
Yuan Yao http://orcid.org/0000-0003-2279-7463

References

[1] Tao G, Wen Z, Jin X, et al. Polygonisation of railway wheels: a critical review. Railw Eng Sci. 2020;28(4):317–345. doi: 10.1007/s40534-020-00222-x
[2] Zhai W, Jin X, Wen Z, et al. Wear problems of high-speed wheel/rail systems: observations, causes, and countermeasures in China. Appl Mech Rev. 2020;72(6):060801. doi: 10.1115/1.4048897
[3] Isacchi G, Ripamonti F, Corsi M. Innovative passive yaw damper to increase the stability and curve-taking performance of high-speed railway vehicles. Veh Syst Dyn. 2023;61(9):2273–2291. doi: 10.1080/00423114.2022.2105242
[4] Li Y, Chi M, Guo Z, et al. An abnormal carbody swaying of intercity EMU train caused by low wheel–rail equivalent conicity and damping force unloading of yaw damper. Railw Eng Sci. 2023;31(3):252–268. doi: 10.1007/s40534-022-00295-w
[5] Yang C, Xu N, Wang W, et al. Self-steering performance of a new bogie with four independently rotating wheels using caster angle. Int J Rail Transp. 2023. doi:10.1080/23248378.2023.2185694.
[6] Yao Y, Li G, Sardahi Y, et al. Stability enhancement of a high-speed train bogie using active mass inertial actuators. Veh Syst Dyn. 2019;57(3):389–407. doi: 10.1080/00423114.2018.1469776
[7] Zhang X, Li H, Cheng J, et al. Adaptive stability mechanism of high-speed train employing parallel inerter yaw damper. Veh Syst Dyn. 2023;61(1):38–57. doi: 10.1080/00423114.2022.2045027
[8] Persson R, Andersson E, Stichel S, et al. Bogie towards higher speed on existing tracks. Int J Rail Transp. 2014;1(2):40–49. doi: 10.1080/23248378.2013.878294
[9] Fu B, Giossi R, Persson R, et al. Active suspension in railway vehicles: a literature survey. Railw Eng Sci. 2020;28(1):3–35. doi: 10.1007/s40534-020-00207-w
[10] Cui D, Wang H, Li L, et al. Optimal design of wheel profiles for high-speed trains. Proc Inst Mech Eng Part F J Rail Rapid Transit. 2013;229(3):248–261. doi: 10.1177/0954409713509979
[11] Spangenberg U, Frohling R, Els PS. Long-term wear and rolling contact fatigue behaviour of a conformal wheel profile designed for large radius curves. Veh Syst Dyn. 2018;57(1):44–63. doi: 10.1080/00423114.2018.1447677
[12] Ye Y, Vuitton J, Sun Y, et al. Railway wheel profile fine-tuning system for profile recommendation. Railw Eng Sci. 2021;29(1):74–93. doi: 10.1007/s40534-021-00234-1

[13] Li G, Li X, Li M, et al. Multi-objective optimisation of high-speed rail profile with small radius curve based on NSGA-II algorithm. Veh Syst Dyn. 2023;61(12):3111–3135. doi: 10.1080/00423114.2022.2158878
[14] Polach O. Wheel profile design for target conicity and wide tread wear spreading. Wear. 2011;271(1–2):195–202. doi: 10.1016/j.wear.2010.10.055
[15] Mohebbi M, Rezvani M. Multi objective optimization of aerodynamic design of high-speed railway windbreaks using lattice boltzmann method and wind tunnel test results. Int J Rail Transp. 2018;6(3):183–201. doi: 10.1080/23248378.2018.1463873
[16] Yao Y, Li G, Wu G, et al. Suspension parameters optimum of high-speed train bogie for hunting stability robustness. Int J Rail Transp. 2020;8(3):195–214. doi: 10.1080/23248378.2019.1625824
[17] Yao Y, Chen X, Li H, et al. Suspension parameters design for robust and adaptive lateral stability of high-speed train. Veh Syst Dyn. 2023;61(4):943–967. doi: 10.1080/00423114.2022.2062012
[18] Chen X, Yao Y, Shen L, et al. Multi-objective optimization of high-speed train suspension parameters for improving hunting stability. Int J Rail Transp. 2022;10(2):159–176. doi: 10.1080/23248378.2021.1904444
[19] Li G, Wu R, Deng X, et al. Suspension parameters matching of high-speed locomotive based on stability/comfort pareto optimization. Veh Syst Dyn. 2022;60(11):3848–3867. doi: 10.1080/00423114.2021.1979602
[20] Chen X, Yao Y, Shen L, et al. Suspension parameter optimal design to enhance stability and wheel wear in high-speed trains. Veh Syst Dyn. 2023;62(5):1230–1252. doi: 10.1080/00423114.2023.2224905
[21] Zou H, Wu Q, Zou X. Research on optimization design of suspension parameters of railway vehicle bogies based on surrogate model. Multimedia Tools Appl. 2022. doi: 10.1007/s11042-022-14022-4
[22] Kalker J. A fast algorithm for the simplified theory of rolling contact. Veh Syst Dyn. 1982;11(1):1–13. doi: 10.1080/00423118208968684
[23] Li J, Liu L, Kou D. Wu Guang high-speed rail track irregularity power spectrum analysis. Appl Mech Mater. 2014;638-640:1224–1228. doi: 10.4028/www.scientific.net/AMM.638-640.1224
[24] Wang C. The characteristic analysis of hollow worn tread of high-speed EMU and its impact on vehicle stability. Disseration, Southwest Jiaotong University.
[25] Sun Y, Zhu S, Zhai W. Influence of tread hollow-worn wheel on wheel/rail interaction. J Mech Eng. 2018;58(4):109–116. in Chinese. doi: 10.3901/JME.2018.04.109
[26] Sun Y, Guo Y, Lv K, et al. Effect of hollow-worn wheels on the evolution of rail wear. Wear. 2019;436-437:203032. doi: 10.1016/j.wear.2019.203032
[27] GB/T 5599-2019. Specification for dynamic performance assessment and testing verification of rolling stock. China: National Railway Administration; 2019.
[28] Bai J, Zeng J, Shi H, et al. Effects of anti-hunting shock absorber on stability of high-speed train. J Vib Shock. 2020;39(23):78–83. in Chinese.
[29] Yang J, Zhou J, Fang R, et al. Multi-objective particle swarm optimization based on adaptive grid algorithms. J Syst Simu. 2008;20(21):5843–5847.
[30] Polach O, Vuitton J. Which parameters determine the type of bogie hunting bifurcation?Lecture Notes in Mechanical Engineering. Springer International Publishing; 2020.
[31] Li H, Yao Y, Chen X, et al. Unstable limit cycle solution for hunting motion of railway vehicle based on initial state excitation method. China Railw Sci. 2023;39(23):78–83. in Chinese.